RESEARCH ARTICLE
PLANETARY SCIENCES

*Earth and Planetary Physics*
*10*: 385–399, 2026
doi: 10.26464/epp2026044

# Characterizing lunar 1 Hz whistler waves across a solar cycle using ARTEMIS observations

**LongFei Jia, Song Fu*, YueQun Lou, TaiFeng Jin, XiaoTong Yun, ShaoTing Cheng, ShuYue Pang, XiangYuan Tong, Xin Ma, and BinBin Ni**

School of Earth and Space Science and Technology, Wuhan University, Wuhan 430072, China

**Key Points:**

- Lunar 1 Hz waves primarily occur in the solar wind near the Moon, showing dawn–dusk and north–south asymmetries, suggesting a link to the distribution of lunar crustal magnetic anomalies and reflected ions.
- Only ~10% of waves are magnetically connected to the Moon, yet their occurrence correlates strongly with lunar magnetic anomalies, indicating a complex generation process not solely reliant on direct connection.
- Wave amplitude increases with the solar wind dynamic pressure and interplanetary magnetic field magnitude and decreases with the Alfvén Mach number, underscoring the significant influence of upstream solar wind conditions on wave properties.

**Citation:** Jia, L. F., Fu, S., Lou, Y. Q., Jin, T. F., Yun, X. T., Cheng, S. T., Pang, S. Y., Tong, X. Y., Ma, X., and Ni, B. B. (2026). Characterizing lunar 1 Hz whistler waves across a solar cycle using ARTEMIS observations. *Earth Planet. Phys.*, *10*(3), 385–399. http://doi.org/10.26464/epp2026044

---

**Abstract:** Whistler-mode waves are ubiquitous in space environments and constitute a key mechanism for energy transfer and transformation. The near-1 Hz narrowband whistler-mode waves are commonly observed in lunar space. However, the generation mechanism of narrowband 1 Hz whistler-mode waves in the lunar environment, where no global magnetosphere or permanent bow shock exists, remains an open question. This study examines 1 Hz waves in the lunar environment by analyzing 12 years (2012–2023) of ARTEMIS (Acceleration, Reconnection, Turbulence, and Electrodynamics of the Moon's Interaction with the Sun) mission data (across an entire solar cycle). The spatial distribution, spectral characteristics, and polarization properties of these waves are investigated alongside their dependence on upstream solar wind parameters and lunar magnetic anomalies. The results reveal that 1 Hz waves are predominantly observed in the solar wind near the Moon, with clear dawn–dusk and north–south asymmetries. Wave amplitudes range from 0.03 to 1 nT, and approximately 90% of the events demonstrate no direct magnetic connectivity to the Moon. Importantly, wave amplitude shows a positive correlation with the solar wind dynamic pressure ($P_{\mathrm{dyn}}$) and the total interplanetary magnetic field ($B_{\mathrm{total}}$) and an inverse correlation with the Alfvén Mach number ($M_{\mathrm{A}}$), underscoring the influence of upstream conditions on wave properties. Our findings reveal that the majority of waves occur on unconnected field lines, indicating a more complex generation and propagation scenario than previously assumed. Furthermore, wave properties are quantitatively shown to be strongly modulated by upstream solar wind conditions. These results provide critical statistical constraints for future studies of wave generation in the unique plasma environment of an unmagnetized body.

**Keywords:** Moon; whistler waves; solar wind; statistical analysis; solar activity cycle

---

## 1. Introduction

Narrowband whistler-mode waves with frequencies near 1 Hz, commonly known as "1 Hz waves," "monochromatic whistler waves," or "upstream whistler waves," are a frequently observed phenomenon in the solar system. They have been detected upstream of various planetary bow shocks, including those of Mercury (e.g., Orlowski et al., 1990, 1995; Russell, 2007; Le et al., 2013), Venus (e.g., Orlowski et al., 1990, 1995; Orlowski and Russell, 1991; Russell, 2007), the Earth (e.g., Russell et al., 1971; Fairfield, 1974; Hoppe et al., 1981, 1982; Orlowski et al., 1990; Orlowski and Russell, 1991; Greenstadt et al., 1995; Balikhin et al., 1997; Tsurutani et al., 2001; Russell, 2007), Mars (Ruhunusiri et al., 2018), Jupiter (Tsurutani et al., 1993), and Saturn (e.g., Orlowski et al., 1995; Russell, 2007; Sulaiman et al., 2017), as well as near the Moon (e.g., Halekas et al., 2006; Tsugawa et al., 2011; Harada et al., 2015; Lou YQ et al., 2023). These waves are typically observed to be left-hand polarized and Doppler shifted (Russell, 2007). This observation suggests that they are intrinsically right-hand polarized waves propagating upstream against the solar wind with a small wave-normal angle. The solar wind flow then advects these waves back toward the observer, resulting in a significant Doppler shift and the observed left-hand polarization. Waves propagating at larger wave-normal angles experience less Doppler shift and retain their intrinsic right-hand polarization (Fairfield, 1974;

---

First author: L. F. Jia, jia.longfei@whu.edu.cn
Correspondence to: S. Fu, fusion@whu.edu.cn
Received 28 SEP 2025; Accepted 11 MAR 2026.

Orlowski and Russell, 1991).

Although 1 Hz waves are commonly associated with bow shock upstream regions at other planets, the Moon's lack of a persistent, well-developed bow shock (although rare, transient bow shock-like structures have been reported; see, e.g., Lin et al., 1998) implies that a different generation mechanism is likely responsible for lunar 1 Hz waves. Despite considerable research, a definitive explanation for the generation of these lunar waves remains elusive. A leading hypothesis involves the interaction of the solar wind with lunar crustal magnetic anomalies. Reflected ions from these anomalies (Tsugawa et al., 2011; Harada et al., 2015) and direct interaction between the solar wind and the crustal magnetic fields (Halekas et al., 2006) are potential sources. Because of the significant mass difference between ions and electrons, and the fact that the typical solar wind proton cyclotron radius near the Moon is comparable to the scale of lunar magnetic anomalies, ion-driven mechanisms are considered more probable (Tsugawa et al., 2011). Furthermore, the energy flux of lunar-reflected ions is approximately 10% greater than that of the incident solar wind ions (Saito et al., 2010), providing a substantial energy source for wave excitation (Tsugawa et al., 2011). Mechanisms typically invoked for upstream waves at other planets, such as foreshock disturbances (Baumgärtel and Sauer, 1995) or energetic electrons reflected by a bow shock (Sentman et al., 1983), are less likely to be relevant at the Moon because of the rarity of bow shock formation.

Observations of lunar 1 Hz waves have been reported by multiple spacecraft missions, including Wind (Farrell et al., 1996), Geotail (Nakagawa et al., 2003), Lunar Prospector (Halekas et al., 2006), Kaguya (Tsugawa et al., 2011), and ARTEMIS (Acceleration, Reconnection, Turbulence, and Electrodynamics of the Moon's Interaction with the Sun; Harada et al., 2015; Lou YQ et al., 2023). Using Wind data, Farrell et al. (1996) observed 1 Hz ultra-low-frequency (ULF) wave activity upstream of the lunar wake, along field lines connected to the wake penumbra. Geotail observations (Nakagawa et al., 2003) revealed similar 1 Hz ULF waves propagating nearly parallel to magnetic field lines connected to the lunar wake. Analysis of 1.5 years of Lunar Prospector Magnetometer data at ~100 km altitude (Halekas et al., 2006) showed a clear correlation between monochromatic whistler waves and lunar crustal magnetic sources, suggesting generation either at a shock-like structure above the anomalies or directly from solar wind interaction. Tsugawa et al. (2011), using one year of Kaguya Lunar Magnetometer data at ~100 km altitude, found that 1 Hz narrowband magnetic fluctuations exhibited a clear dependence on the solar zenith angle, including north–south and dawn–dusk asymmetries. They proposed that these waves are generated by the interaction of the solar wind with lunar crustal magnetic anomalies, with reflected ion beams serving as a potential energy source. Harada et al. (2015) analyzed 3.5 years of ARTEMIS Fluxgate Magnetometer (FGM) data from ~1.1–12 lunar radii ($R_L$) and demonstrated that the 1 Hz magnetic field fluctuations are influenced by both the upstream magnetic field direction and the Alfvén Mach number. Wave intensity was enhanced on the dawn side during periods of Parker spiral interplanetary magnetic field (IMF) configuration, coinciding with increased Moon-related ion flux, and the waves extended further upstream during low Mach number conditions. Lou YQ et al. (2023) found that lunar 1 Hz narrowband whistler-mode waves exhibited moderate day–night and dawn–dusk asymmetries, as well as a slight north–south asymmetry, suggesting a connection to lunar magnetic anomalies. These waves were notably absent inside the Earth's magnetosphere. On the lunar dayside, the waves were more intense and had lower peak frequencies. Stronger waves were generally associated with smaller wave-normal angles and stronger left-hand polarization.

This study aims to further characterize lunar 1 Hz waves and investigate their generation mechanisms by using data from the ARTEMIS mission. Previous studies, such as Lou YQ et al. (2023), provided valuable statistical results based on a few years of data, which primarily reflected conditions during a specific phase of solar activity. Our extended temporal coverage allows us to (1) leverage a full solar cycle dataset (2012–2023) to move beyond snapshots of specific solar activity levels and establish a long-term, statistically robust baseline for wave properties; (2) systematically decouple solar cycle variations from intrinsic spatial distributions, allowing for a clearer understanding of how both large-scale solar drivers and local lunar conditions shape the wave environment; and (3) quantitatively link wave properties to a comprehensive set of upstream solar wind parameters to build a predictive understanding of how these waves respond to their plasma environment and solar activity. Section 2 provides details on the ARTEMIS mission, the instruments used, the criteria for wave event selection, and a representative case study. Section 3 presents a statistical analysis of lunar 1 Hz waves observed over a complete solar cycle. This analysis explores the relationship between these waves and lunar magnetic anomalies, as well as the dependence of wave amplitude and peak frequency on various solar wind parameters. Section 4 summarizes the key findings and discusses their implications.

## 2. Data and Method

In this study, we utilize data from the ARTEMIS mission (Angelopoulos, 2011), a spin-off of the THEMIS (Time History of Events and Macroscale Interactions during Substorms) mission. ARTEMIS consists of two probes (P1 and P2) in near-ecliptic orbits with inclinations ranging from 0° to 30°. The probes have an orbital period of approximately 26 hours and are located at selenocentric distances ranging from ~1.1 to 12 $R_L$, which corresponds to ~55–65 Earth radii ($R_E$) geocentric distance. We analyze magnetic field and particle data from the ARTEMIS P2 probe, collected between January 1, 2012, and December 31, 2023, to investigate 1 Hz waves in the lunar environment.

Magnetic field vector data are provided by the FGM instrument (Auster et al., 2008). We use level "L2" data of the FGM. To analyze the magnetic field perturbations, we transform the magnetic field data from Geocentric Solar Ecliptic (GSE) coordinates into a field-aligned coordinate system. First, we define the background magnetic field vector, $\boldsymbol{B}_0$, as the 600-second running average of the magnetic field. The field-aligned coordinate system is then constructed as follows: The parallel component, $B_{//}$, is defined to be parallel to the background field vector $\boldsymbol{B}_0$. The first perpendicular component is defined as $B_{\perp 1} = (B_{/\!/} \times \boldsymbol{X}_{\mathrm{GSE}}) / |B_{/\!/} \times \boldsymbol{X}_{\mathrm{GSE}}|$, where $\boldsymbol{X}_{\mathrm{GSE}}$ is the unit vector pointing sunward. The second perpendicular component, $B_{\perp 2}$, completes the right-handed orthogonal system, defined as $B_{\perp 2} = B_{/\!/} \times B_{\perp 1}$. We then apply the fast Fourier transform (FFT) to the magnetic field data, sliding a 32-second Hamming window by 8 seconds. We use SPEDAS (Space Physics Environment Data Analysis System; Angelopoulos et al., 2019) to transform the coordinates, make the transformation matrix, calculate the rotation against the field, and perform an FFT.

Ion energy spectra and the particle moments (ions density and velocity) are provided by the Electrostatic analyzer (ESA) instrument (McFadden et al., 2008). We use the ion density and velocity to calculate the solar wind parameters (dynamic pressure [$P_{\mathrm{dyn}}$], velocity [$V_{\mathrm{SW}}$], and Alfvén Mach number [$M_{\mathrm{A}}$]).

To ensure the robust identification of 1 Hz waves, we apply the following selection criteria:

(1) *Frequency range*: Events with peaks in the power spectral density within the frequency range of 0.6–4 Hz are selected. For data collected between 2012 and 2015, where the Nyquist frequency is limited to 4 Hz, the upper limit is adjusted to 2 Hz. The lower bound of 0.6 Hz is chosen to exclude spin tones and their second harmonics (Harada et al., 2015).

(2) *Power threshold*: Events with power spectral density peaks exceeding 0.01 $\mathrm{nT}^2/\mathrm{Hz}$ are retained to minimize contamination from instrumental noise (Lou YQ et al., 2023).

(3) *Drop level*: The drop level, defined as the ratio (in decibels) between the peak intensity and the minimum intensity within the frequency range of 0.6 Hz to the peak frequency (Tsugawa et al., 2011), is required to exceed 10 dB. The threshold of 10 dB is set to preserve narrowband waves while ensuring their continuity and integrity.

(4) *Ellipticity*: Only events with ellipticity values less than 0 are selected to focus on left-hand polarized waves, thereby excluding right-hand broadband magnetic turbulence.

(5) *Wave-normal angle*: Events with wave-normal angles below 60° are included to ensure higher accuracy, consistent with previous statistical studies (Lou YQ et al., 2023).

Finally, we perform visual inspection of the spectrograms to exclude broadband magnetic turbulence that might be spectrally close to the 1 Hz waves. Applying these criteria, we identify 37,983 1 Hz wave data points over the 12-year period.

Figure 1 presents a representative example of a 1 Hz wave event observed on July 31, 2022. The data are presented in Selenocentric Solar Ecliptic (SSE) coordinates, which are Moon-centered, where the *X*-axis points toward the Sun, the *Y*-axis points toward dusk, and the *Z*-axis is parallel to the ecliptic pole. Figure 1a shows the energy spectrum of all ions, whereas Figure 1b shows the energy spectrum of non-solar wind ions. Non-solar wind ions are identified based on their energy per charge ($E/q$) and angle relative to the solar wind velocity. Ions with $E/q$ between 0.4 $E_{\mathrm{SW}}/e$ (where $E_{\mathrm{SW}}/e$ is the solar wind proton energy per charge) and 4 $E_{\mathrm{SW}}/e$, and with angles within 45° of the solar wind velocity direction, are classified as solar wind ions (Howard et al., 2017); all other ions are considered non-solar wind ions (Harada et al., 2015). Figures 1a and 1b reveal a flux enhancement of reflected ions in the energy range of 100–1000 eV. Figure 1c displays the magnetic power spectral density, showing the presence of 1 Hz waves from 02:04 to 02:32 universal time (UT), with a peak frequency near 1.5 Hz. Figures 1d and 1e show the wave-normal angle and ellipticity, respectively, confirming that the waves are quasi-parallel propagating and left-hand polarized. Figure 1f presents the filtered magnetic field data for the wave event. Figures 1f and Figure 1g compare the filtered results by different thresholds. Figure 1h shows the drop level in the wave event, which is mostly above 10 dB, although part of the waves could be beyond the 20 dB threshold. Figure 1i shows the power-weighted wave-normal angle, which is below 60°, and the power-weighted ellipticity, which ranges from approximately −0.7 to −0.5. The power-weighted wave-normal angle and ellipticity are calculated by using the method described by Yu J et al. (2017; Equation (2)). Figure 1j shows the integrated wave amplitude, which varies between 0.2 and 0.8 nT during this event. This example illustrates the typical characteristics of 1 Hz waves observed in the lunar environment, providing a foundation for the subsequent statistical analysis.

The 10 dB threshold for the drop level is adapted from previous studies (e.g., Tsugawa et al., 2011), which often used a more stringent 20 dB criterion. As noted by Lou YQ et al. (2023), a 20 dB threshold can be overly restrictive and may lead to an underestimation of wave occurrence by breaking continuous wave events into disconnected segments. Our tests (Figure 1) confirm that a 10 dB threshold is more effective at identifying complete, continuous narrowband events. Although a lower threshold can potentially pick up more noise, we mitigate this by performing a final visual inspection of all identified events to exclude broadband turbulence or instrumental noise.

## 3. Results

### 3.1 Spatial Distribution of 1 Hz Waves

Figure 2 presents the spatial occurrence rate of 1 Hz waves observed over a complete solar cycle. We merge all available data with a resolution of $1.5 \times 1.5\ R_{\mathrm{E}}$ in the *X*–*Y* planes in GSE coordinates and $1.5 \times 0.2\ R_{\mathrm{E}}$ in the *X*–*Z* planes in GSE coordinates, $0.25 \times 0.25\ R_{\mathrm{L}}$ in the *X*–*Y* planes of SSE coordinates, $0.25 \times 0.1\ R_{\mathrm{L}}$ in the *X*–*Z* planes of SSE coordinates. Here $R_{\mathrm{E}}$ is radius of earth and $R_{\mathrm{L}}$ is radius of moon. The spatial occurrence in each bin is defined as the ratio between the number of 1 Hz wave data points to the total number of satellite samples regardless of the presence of 1 Hz waves. The occurrence rate generally ranges from 0.05% to 10%. Figures 2a and 2b display the occurrence rates in the *X*–*Y* and *X*–*Z* planes, respectively, in GSE coordinates. In GSE coordinates, the *X*-axis points sunward, the *Y*-axis points duskward (opposite to planetary orbital motion), and the *Z*-axis is parallel to the ecliptic pole. Figures 2c and 2d show the occurrence rates in SSE coordinates. The black line and dashed black line in Figure 2a represent the boundaries of the magnetosheath (Slavin and Holzer, 1981; Equation (7)) and magnetopause (Shue et al., 1997; Equation (1)), respectively. The magnetopause and bow shock here are drawn for average solar wind conditions: Magnetosheath boundary (bow shock): $V_{\mathrm{SW}} = 400$ km/s; $n_{\mathrm{p}} = 5\ \mathrm{cm}^{-3}$; $B = 6$ nT; $T_{\mathrm{p}} =$

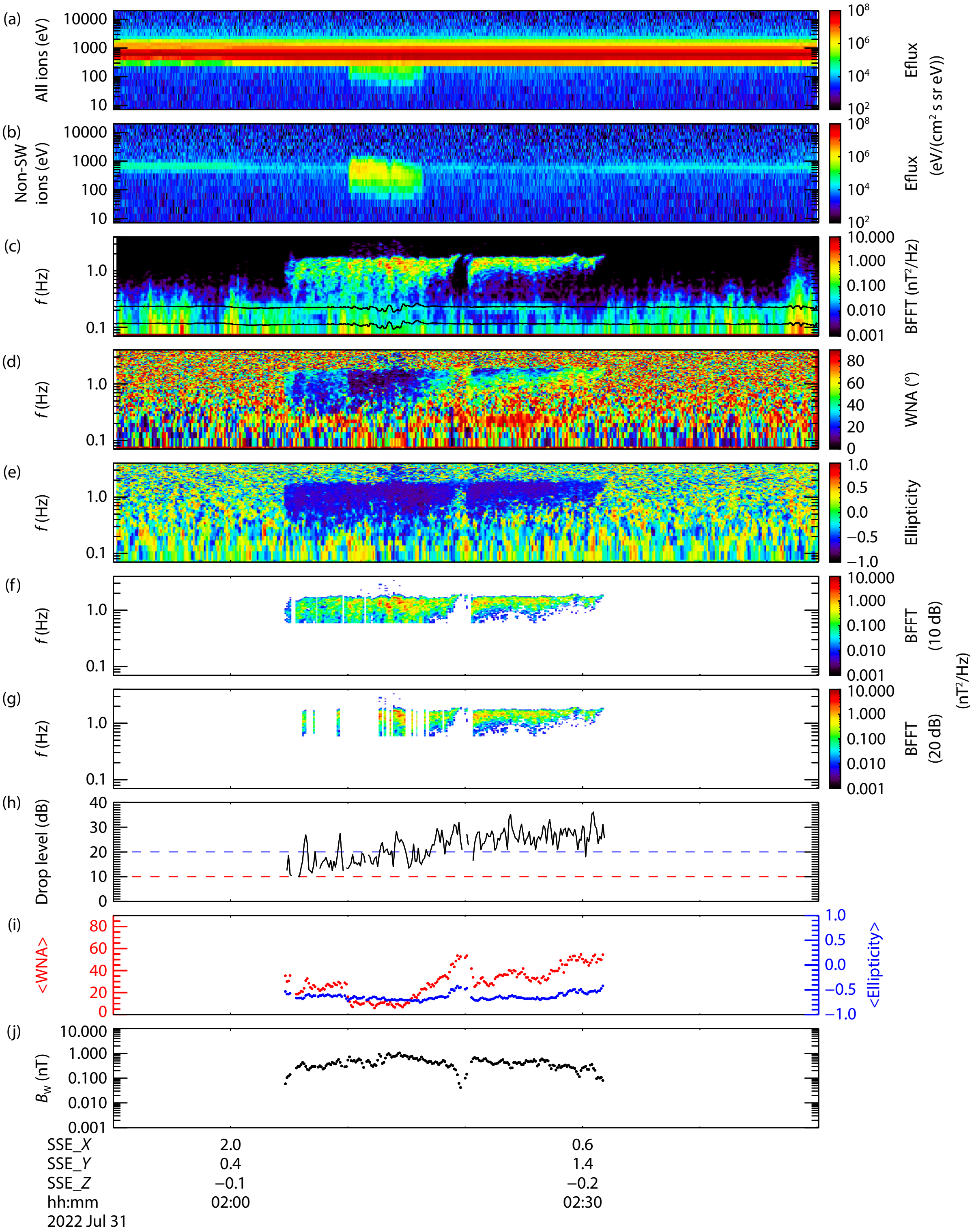

**Figure 1**. Example of a 1 Hz wave event observed by ARTEMIS P2 on July 31, 2022. (a) Ion energy spectrogram (all ions). (b) Ion energy spectrogram (non-solar wind ions). (c) Magnetic field power spectral density, which was calculated from the magnetic field data using the fast Fourier transform (FFT). The lower and upper black curves indicate the fundamental proton cyclotron frequency ($f_{cp}$) and its second harmonic (2 $f_{cp}$), respectively. (d) Wave-normal angle (WNA). (e) Ellipticity. (f) Bandpass-filtered magnetic field power spectral density in the 1 Hz wave frequency range with 10 dB threshold. (g) Bandpass-filtered magnetic field power spectral density in the 1 Hz wave frequency range with a 20 dB threshold. (h) Drop level of the 1 Hz waves with a 10 dB threshold. The dotted blue line marks 20 dB, and the dotted red line marks 10 dB. (i) Power-weighted wave-normal angle (red dots) and ellipticity (blue dots) for the identified 1 Hz wave. (j) Wave amplitude $B_w$.

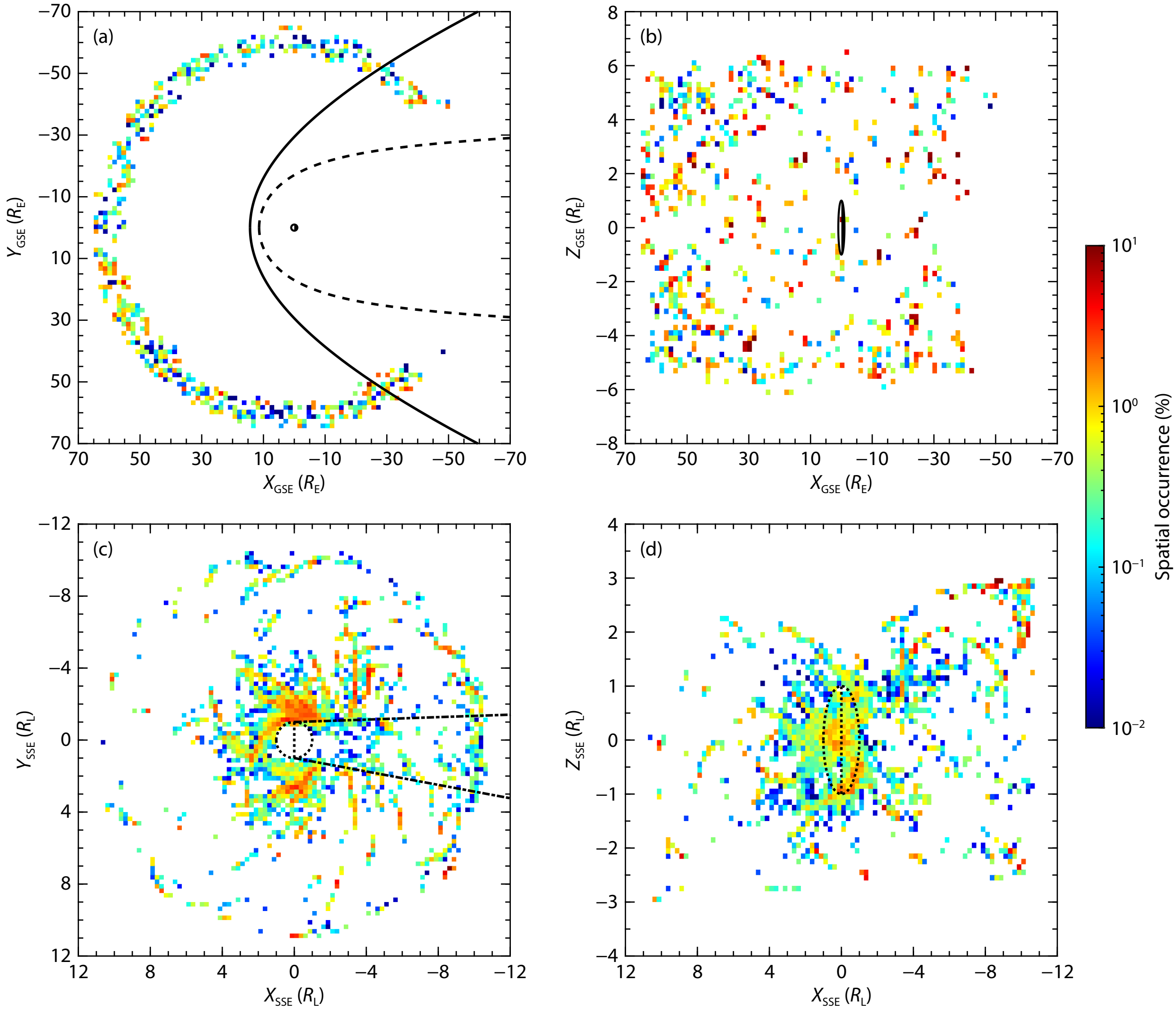

**Figure 2**. Spatial distribution of the 1 Hz wave occurrence rates in the (a) *X–Y* and (b) *X–Z* planes of Geocentric Solar Ecliptic (GSE) coordinates, and (c) *X–Y* and (d) *X–Z* planes of Selenocentric Solar Ecliptic (SSE) coordinates. In panel (a), the black line represents the average magnetosheath boundary (Slavin and Holzer, 1981; Equation (7)), and the dashed black line represents the average magnetopause (Shue et al., 1997; Equation (1)). In panel (c), the dashed-dotted black lines represent the lunar wake boundary. The black circle and ellipse at the centers of panels (a) and (b) represent the Earth, with the filled semicircle indicating the nightside and the open semicircle indicates the dayside. The dotted circle and ellipse at the centers of panels (c) and (d) represent the Moon, with dotted black lines divided it into dayside ($X_{SSE} > 0$) and nightside ($X_{SSE} < 0$).

$8 \times 10^4$ K; $T_e = 15 \times 10^4$ K (Slavin and Holzer, 1981); Magnetopause: $V_{SW} = 400$ km/s; $n_p = 5$ cm$^{-3}$; IMF $B_z = 0$ nT (Shue et al., 1997). Here $n_p$ is proton density, $T_p$ is proton temperature and $T_e$ is electron temperature. Consistent with Lou YQ et al. (2023), almost no waves are observed for $X_{GSE} < -45\ R_E$. In Figure 2c, a dawn–dusk asymmetry is evident near the Moon, with higher occurrence rates (warmer colors) on the dawn side ($Y_{SSE} < 0$) within $|X_{SSE}| < 2\ R_L$, with a notable absence near the lunar wake (represented as dashed-dotted black lines) and at an angle of 12.5° backwards of the solar wind direction (Zhang H et al., 2014). Considering that the SSE coordinate is a Moon-centered system and that the Moon also revolves around the Sun, we apply a typical solar wind velocity (~400 km/s along the $-X_{SSE}$ direction) and the Moon's aberration velocity (~29.8 km/s along the $-Y_{SSE}$ direction). To determine the actual direction of the solar wind when applying the aberration, the aberration velocity has been added back to the $+Y_{SSE}$ direction of the solar wind velocity (Zhang H et al., 2019). A dawn–dusk asymmetry is evident near the Moon, with higher occurrence rates on the dawn side ($|X_{SSE}| < 2\ R_L$ and $|Y_{SSE}| < 3\ R_L$). Note the enhanced occurrence on the dawn flank, which is consistent with the interaction between the solar wind and the lunar wake. However, at $\sqrt{X_{SSE}{}^2 + Y_{SSE}{}^2} = \sim 11\ R_L$, the occurrence rate is higher on the nightside. Figure 2d shows that near the Moon, 1 Hz waves are concentrated around the equator, but their distribution expands to higher $Z_{SSE}$ with increasing $X_{SSE}$, Interestingly, for $|X_{SSE}| < 1\ R_L$, the occurrence rate is higher in the southern hemisphere, while this asymmetry reverses at $X_{SSE} \sim 10\ R_L$. The data are not uniformly distributed in the *X–Y* plane of SSE coordinates. The satellite provides more samples at ~11 $R_L$ and region within ~4 $R_L$, which is caused by the orbit design of ARTEMIS. The satellite dwells for a longer time near the apoapsis. More samples at ~11 $R_L$ provide details about the difference in wave occurrence on the dayside and on the nightside. The high occurrence on the nightside may be correlated with the distribution of Moon-related ions. The Moon-related ions originate from the dayside and are convected downstream (Harada et al., 2015). However, the absence of Moon-related ions on the upstream solar wind (like dayside at ~11 $R_L$) may lead to the lower occurrence of 1 Hz waves. Furthermore, as mentioned above, the satellite dwells for a longer time near the apoapsis. The number of samples in the range of 4–11 $R_L$ is generally lower, leading to fewer waves being observed in that region.

Figure 3 shows the spatial distribution of the 1 Hz wave average amplitude. The wave amplitudes generally range from 0.03 to 1 nT. Figures 3a and 3b show slightly stronger amplitudes in the terrestrial magnetosheath ($X_{GSE} < -30\ R_E$) and no significant features in the $X$–$Z$ plane. In Figure 3c, warmer colors indicate a higher amplitude and are clearly concentrated near the Moon ($X_{SSE} = 0$ to $-2\ R_L$). The figure reveals that wave amplitudes are strongest in close proximity to the Moon, and many high-amplitude waves are observed at $\sqrt{X_{SSE}{}^2 + Y_{SSE}{}^2} = \sim 11\ R_L$. Day–night, dawn–dusk, and north–south asymmetries are present, with stronger amplitudes on the dayside, dawn side, and northern hemisphere, respectively. In Figure 3d, the most intense waves are seen in the northern dayside region (top-left quadrant near the Moon), followed by the southern nightside region (bottom-right quadrant near the Moon). Amplitudes in these regions are significantly higher than in surrounding areas and peak near the equator. Last, we calculate the ratio between wave parameters on the dusk side ($Y_{SSE} > 0$) and those on the dawn side ($Y_{SSE} < 0$). The dawn–dusk asymmetric ratio is 0.64 for occurrence, 0.73 for $B_w$ (wave amplitude) and 0.97 for peak frequency. We also calculate the ratio between wave parameters on the northern hemisphere ($Z_{SSE} > 0$) and those on the southern hemisphere ($Z_{SSE} < 0$) for $|Z_{SSE}| < 1\ R_L$. The north–south asymmetric ratio is 0.88 for occurrence and 0.94 for $B_w$. Furthermore, regardless of the limit of $|Z_{SSE}|$, the north–south asymmetric ratio of $B_w$ is 0.86.

Figures 4 and 5 display the spatial distributions of 1 Hz wave average ellipticity and average wave-normal angle, respectively. These parameters exhibit similar distribution patterns. Ellipticity values primarily range from −0.7 to −0.45, and wave-normal angles are generally around 30°. No distinct distribution features are observed in GSE coordinates (Figures 4a, 4b, and 5a, 5b). In SSE coordinates (Figures 4c, 4d, and 5c, 5d), waves near the Moon $\left(\left|\sqrt{X^2_{SSE} + Y^2_{SSE}}\right| < \sim 2\ R_L\right)$ tend to be more linearly polarized and

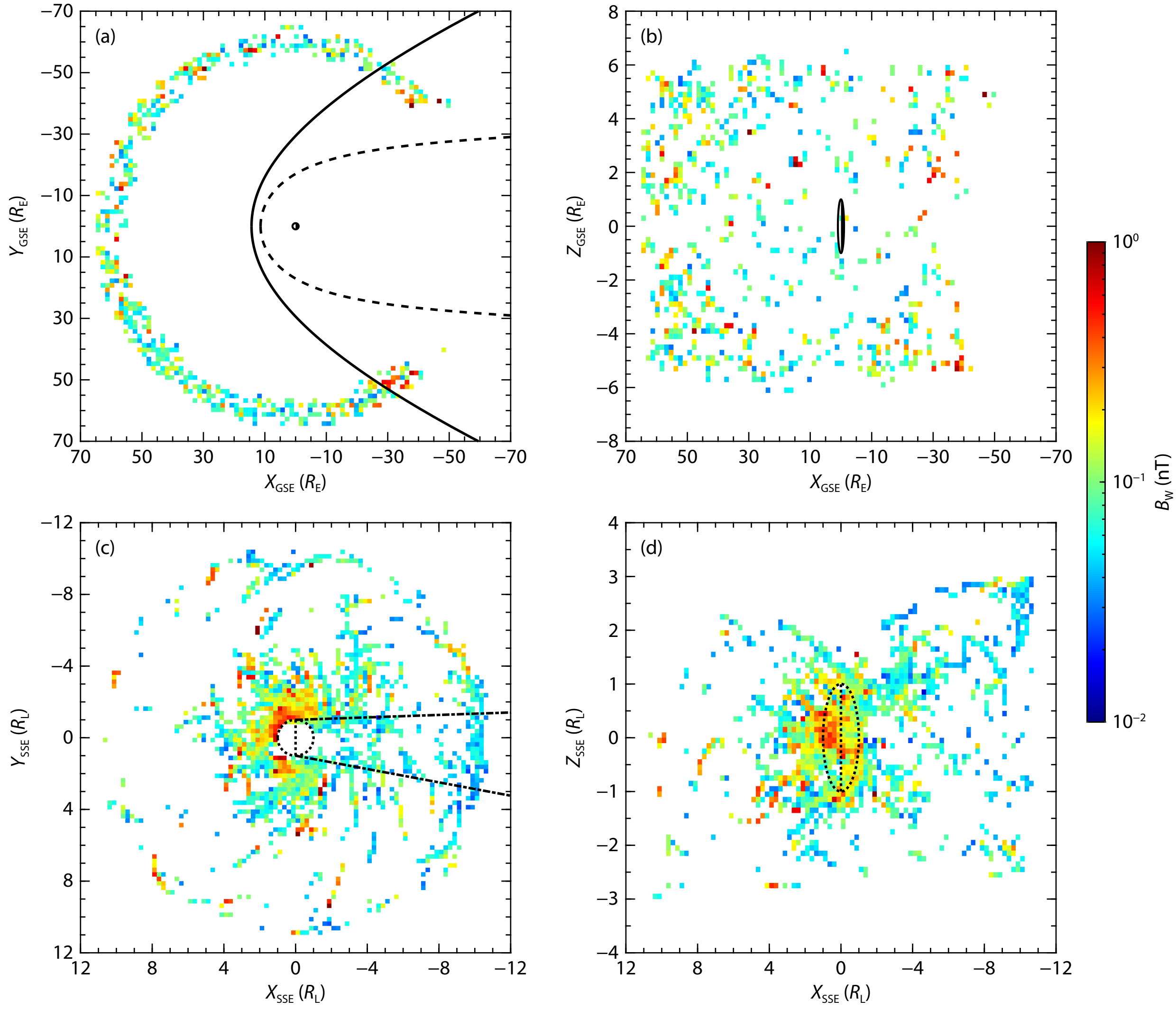

**Figure 3**. Spatial distribution of the 1 Hz wave amplitude in the same format as Figure 2.

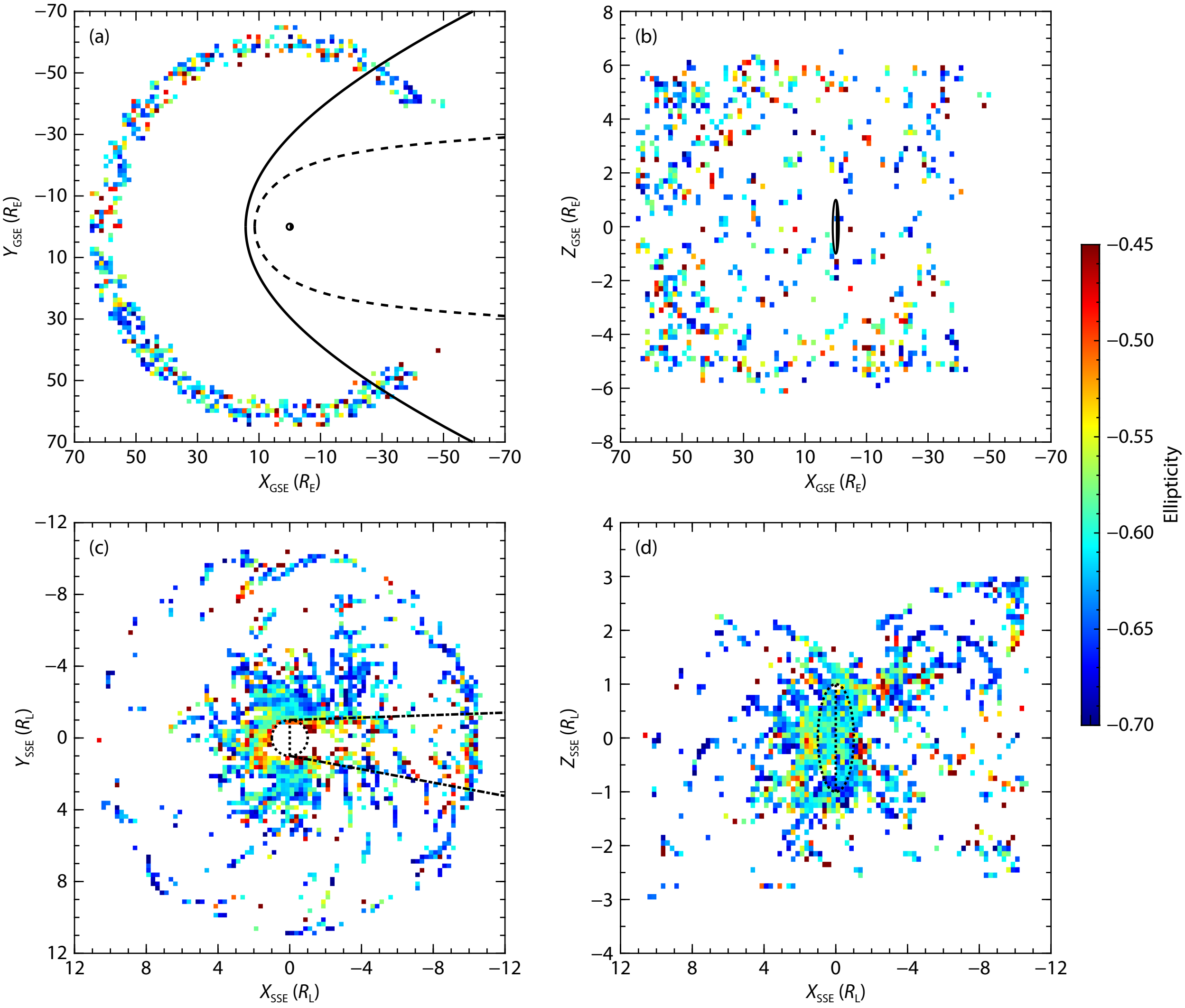

**Figure 4**. Spatial distribution of the 1 Hz wave ellipticity in the same format as Figure 2.

propagate more perpendicularly. Specifically, on the dayside and around the lunar wake (about $X_{SSE} < 0\ R_L$ and $|Y_{SSE}| < 2\ R_L$), waves become increasingly left-hand polarized (cooler colors) and exhibit more parallel propagation (cooler colors) with increasing $|Y_{SSE}|$ in the $X$–$Y$ plane. A similar trend is observed in the $X$–$Z$ plane, with increasing left-hand polarization and parallel propagation at larger radial distances from the Moon.

Figure 6 shows the spatial distribution of the average peak frequency of 1 Hz waves, which generally ranges from 0.6 to 2 Hz. No clear features are apparent in GSE coordinates (Figures 6a and 6b). In the $X$–$Y$ plane of SSE coordinates (Figure 6c), the peak frequency increases with decreasing $|Y_{SSE}|$ and peaks near the lunar wake ($X_{SSE} < 0$ and $|Y_{SSE}| < 2\ R_L$). A slight dawn–dusk asymmetry is present, with higher frequencies (warmer colors) on the dawn side ($|X_{SSE}| < 2\ R_L$ and $|Y_{SSE}| < 3\ R_L$). In the $X$–$Z$ plane (Figure 6d), peak frequencies are higher at $Z_{SSE} = \sim 0.3\ R_L$ than at the equator. Previous studies have suggested a correlation between 1 Hz waves and lunar magnetic anomalies (Tsugawa et al., 2011; Lou YQ et al., 2023). To investigate this relationship, we trace the magnetic field lines from the spacecraft position by using a straight field line approximation, based on the measured magnetic field vector (Harada et al., 2014, 2015; Sawaguchi et al., 2022). We find that only 3504 out of 37,983 1 Hz wave data points (approximately 10%) have background magnetic field lines connecting to the Moon. This result indicates that the majority of lunar 1 Hz waves are observed in regions where the background magnetic field is not connected to the Moon.

Figure 7 presents the spatial distributions of wave properties as a function of longitude and latitude in SSE coordinates. Figures 7a–7f show the results for all waves, regardless of the background magnetic field line connection, whereas Figures 7g–7l show the results for waves with background magnetic field lines connected to the Moon. Figure 7a shows all satellite samples, irrespective of the magnetic field line connection. Figure 7b shows that more 1 Hz waves are observed on the dawn side (−135° to −90° longitude), with a moderate dawn–dusk asymmetry. The spatial occurrence rate peaks at higher latitudes (|20°| to |30°|) on both the dawn side and dusk side. Figure 7c shows that 1 Hz wave amplitudes range from 0.05 to 1 nT. Amplitudes are also more intense on the dawn side in the southern hemisphere, exhibiting both dawn–dusk and slight south–north asymmetries. Figure 7d shows the ellipticity of 1 Hz waves. Waves near the terminators (around

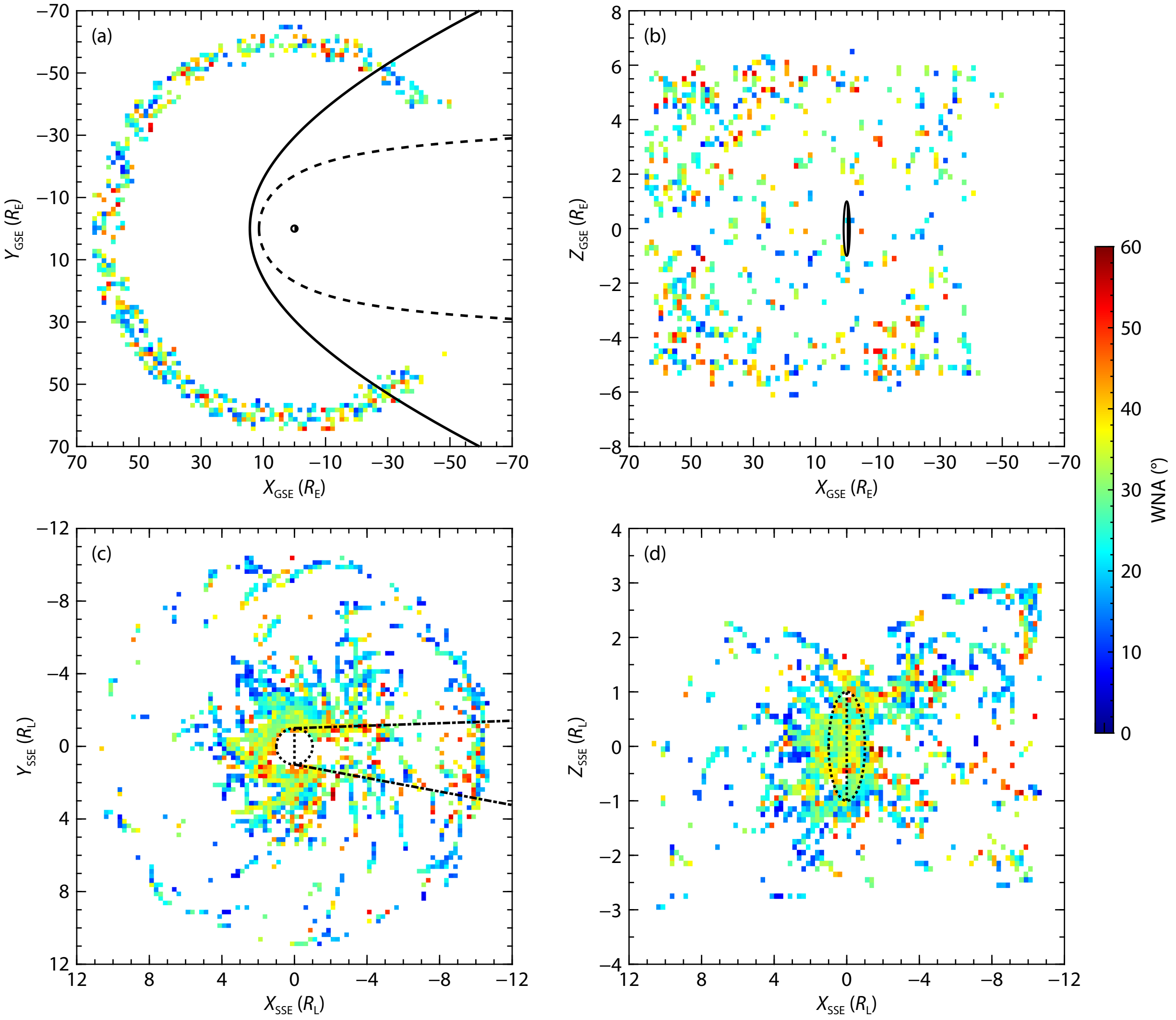

**Figure 5**. Spatial distribution of the 1 Hz wave-normal angle in the same format as Figure 2.

−90° longitude for dawn and 90° longitude for dusk) tend to be more left-hand polarized compared with those at midday (around 0° longitude) and midnight (around 180° longitude). Figure 7e shows the wave-normal angle. Waves tend to propagate more perpendicularly on the nightside (longitude >0°) than on the dayside (longitude < 0°). No obvious features are apparent in the peak frequency distribution, as shown in Figure 7f. Figure 7g shows the satellite samples with background magnetic field lines connected to the Moon. More field lines connect to the Moon around −90° to 0° for the dawn side and 90°–180° for the dusk side. Figure 7h shows that most waves with connected field lines are concentrated on the dayside and dawn side (longitude range from −90° to 45°). No clear latitude distribution is observed. Figure 7i shows that the amplitudes of waves with connected field lines are more intense on the dawn side, especially close to the terminator, peaking at 1 nT. Amplitudes increase as the longitude approaches −90° (dawn terminator). Figures 7j–7l show the ellipticity, wave-normal angle, and peak frequency for waves with connected field lines, but no distinct features are observed. Because waves with background magnetic field line connections represent a small fraction of the total, and total distributions are largely similar to those without connections, we focus our subsequent analysis on the full dataset, regardless of the magnetic field line connection.

Figure 8 shows the spatial distributions of wave properties as a function of the selenographic location of the field line footpoint for events where the background magnetic field line intersects the Moon. Figure 8a shows the total observation samples, regardless of the presence of 1 Hz waves. These samples are concentrated near the equator and are not uniformly distributed in longitude owing to the geometric constraints of the lunar orbit. Figure 8b shows the spatial occurrence rate of 1 Hz waves, ranging from 0.05% to 4%. A clear relationship between the occurrence rate and magnetic anomalies is evident, consistent with Tsugawa et al. (2011), providing further evidence for the role of magnetic anomalies in the generation of 1 Hz waves. Figure 8c shows the average amplitude of 1 Hz waves, ranging from 0.03 to 1 nT. The amplitudes are clearly correlated with the location of magnetic anomalies, with higher amplitudes (typically > ~0.3 nT) observed near regions of high magnetic intensity. Moreover, higher amplitudes can be found in low-latitude regions (<30°). Figure 8d shows the ellipticity of 1 Hz waves. Compared with Figure 8c,

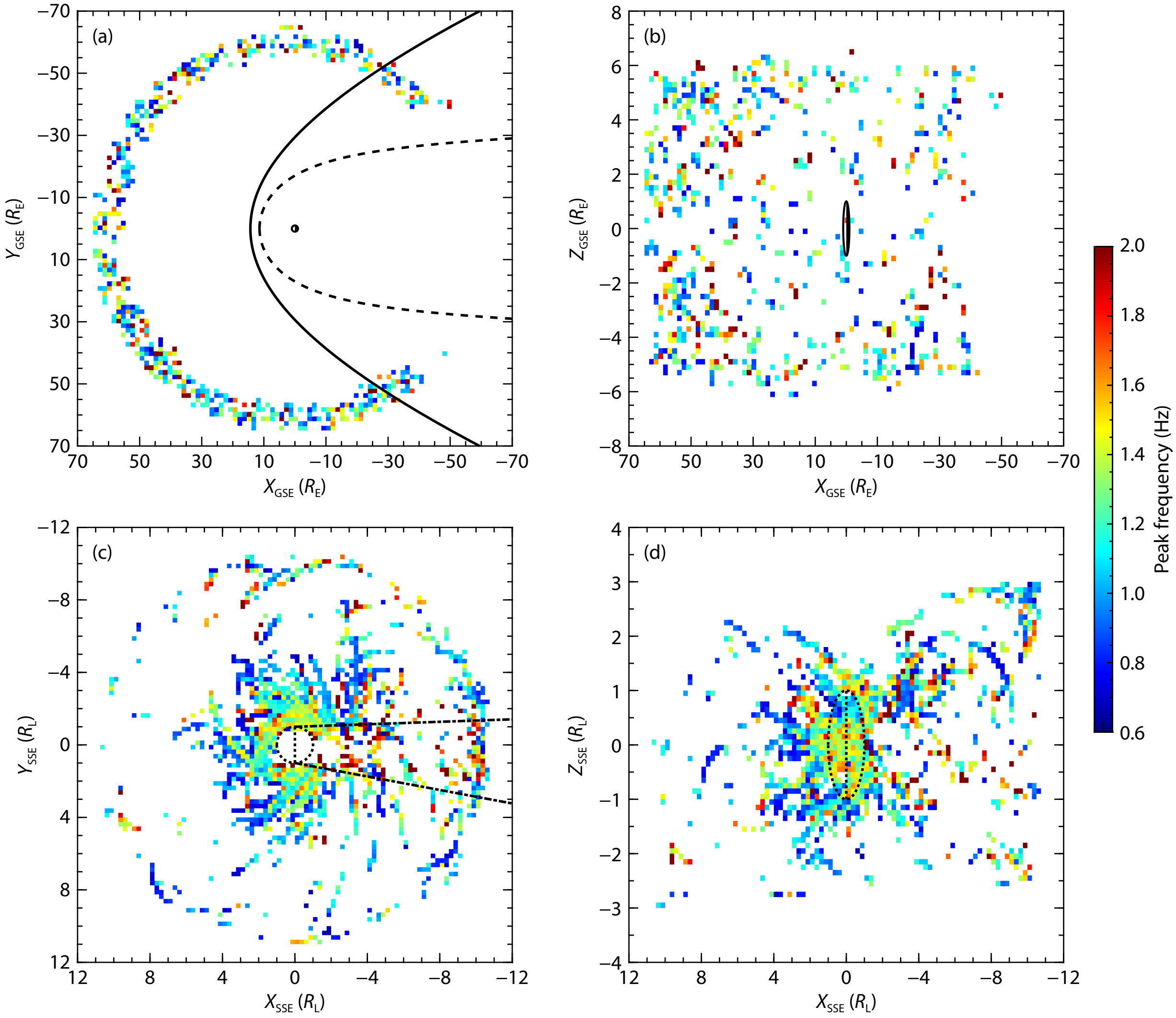

**Figure 6**. Spatial distribution of the 1 Hz wave peak frequency in the same format as Figure 2.

waves tend to be more linearly polarized in regions where the wave amplitude is weaker. Ellipticity is also higher in the southern hemisphere than in the northern hemisphere. Figure 8e shows the wave-normal angle, which exhibits a distribution similar to that of ellipticity. No distinct features are observed in the peak frequency distribution in Figure 8f.

### 3.2 Dependencies of 1 Hz Waves on Solar Wind Parameters and the Solar Cycle

Utilizing 12 years of ARTEMIS observations spanning a full solar cycle, we investigate the temporal evolution of 1 Hz waves and their relationship to the solar cycle. The $F_{10.7}$ index (10.7 cm solar radio flux) comes from the OMNI dataset. Figure 9 presents the occurrence rate of 1 Hz waves (monthly ratio of wave events to satellite samples) alongside the $F_{10.7}$ index, a proxy for solar activity. As shown in Figure 9a, the occurrence rate exhibits pronounced variability over the study period, ranging from ~0% to 0.8%, with a median value of ~0.2%. Notably, minima in occurrence are observed in 2014 and 2022, contrasting with a prominent peak in 2016. From 2015 to 2021, the occurrence displays annual cyclic fluctuations coinciding with $F_{10.7}$ values <100. During the 2021–2024 period, a positive correlation emerges between occurrence and $F_{10.7}$. Figure 9b shows that the wave amplitude varies between 0.08 and 0.4 nT. Data scarcity during the 2013–2015 period limits the robustness of amplitude statistics in this interval. The correlation coefficient between $F_{10.7}$ and occurrence is −0.07 and the correlation coefficient between $F_{10.7}$ and $B_w$ is −0.18. No obvious correlation exists between amplitude and $F_{10.7}$ spanning a full solar cycle. Only a positive correlation emerges between occurrence and $F_{10.7}$ during the 2021–2024 period.

Figure 10 delineates the wave occurrence dependence on key solar wind parameters: dynamic pressure ($P_{dyn}$), velocity ($V_{SW}$), IMF magnitude ($B_{total}$), and Alfvén Mach number ($M_A$). On the basis of the ion density and velocity obtained by the ESA instrument, we regard the solar wind ion velocity as $V_{SW}$. Ions whose angles within 45° of the solar wind velocity direction are classified as solar wind ions (Howard et al., 2017). The $P_{dyn}$ and $M_A$ are calculated by the ion velocity and density. The IMF $B_{total}$ is obtained from the mean of 8-second averaged magnetic field vectors by the FGM instrument. The waves occur preferentially under moderate solar wind conditions: $P_{dyn}$ = 1–1.5 nPa (Figure 10a), $V_{SW}$ = 350–400 km s$^{-1}$ (Figure 10b), $B_{total}$ = 4–6 nT (50% of events; Figure 10c), and

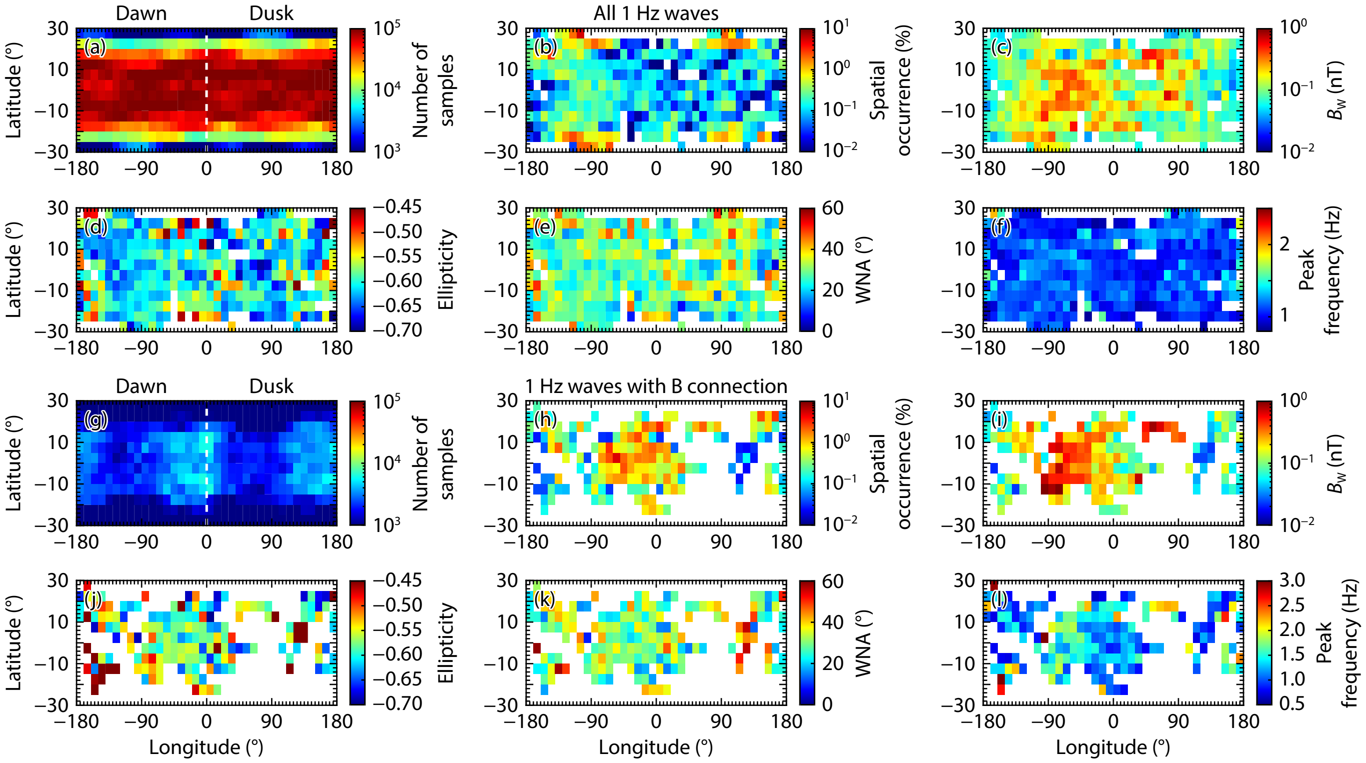

**Figure 7**. Spatial distributions in SSE coordinates, binned by longitude and latitude: (a, g) Number of satellite observation points; (b, h) 1 Hz wave occurrence rates; (c, i) average wave amplitude; (d, j) ellipticity; (e, k) wave-normal angle (WNA); (f, l) peak frequency. Panels (a) to (f) show data for all waves, regardless of magnetic connectivity to the Moon. Panels (g) to (l) show data only for waves with magnetic field lines connected to the Moon.

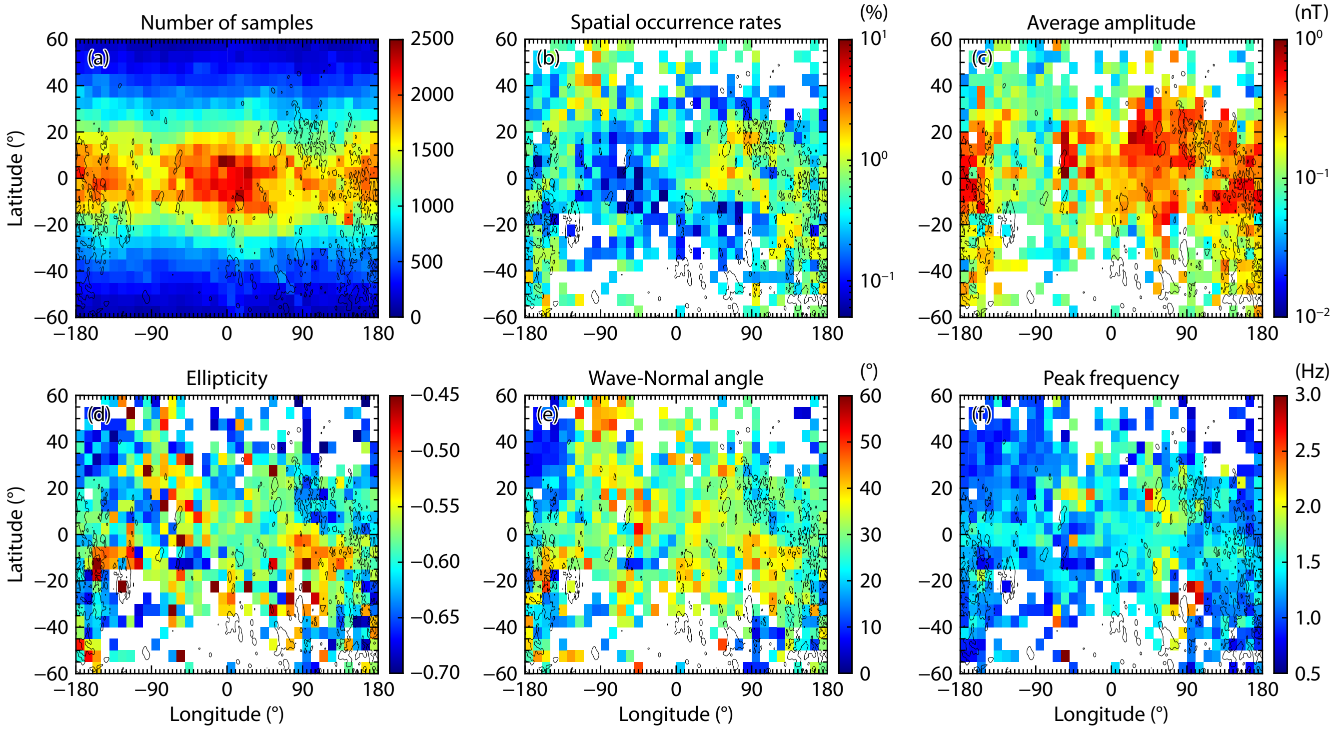

**Figure 8**. Spatial distributions in selenographic coordinates, showing properties of 1 Hz waves with magnetic field lines connected to the Moon: (a) Number of satellite observation points, binned by the selenographic location of the field line footpoint; (b) occurrence rates; (c) average amplitude; (d) ellipticity; (e) wave-normal angle; (f) peak frequency. The black contours represent a crustal magnetic field magnitude of 2 nT at 30 km altitude, derived from the lunar magnetic anomaly model of Tsunakawa et al. (2015); they mark the locations of strong magnetic anomaly zones.

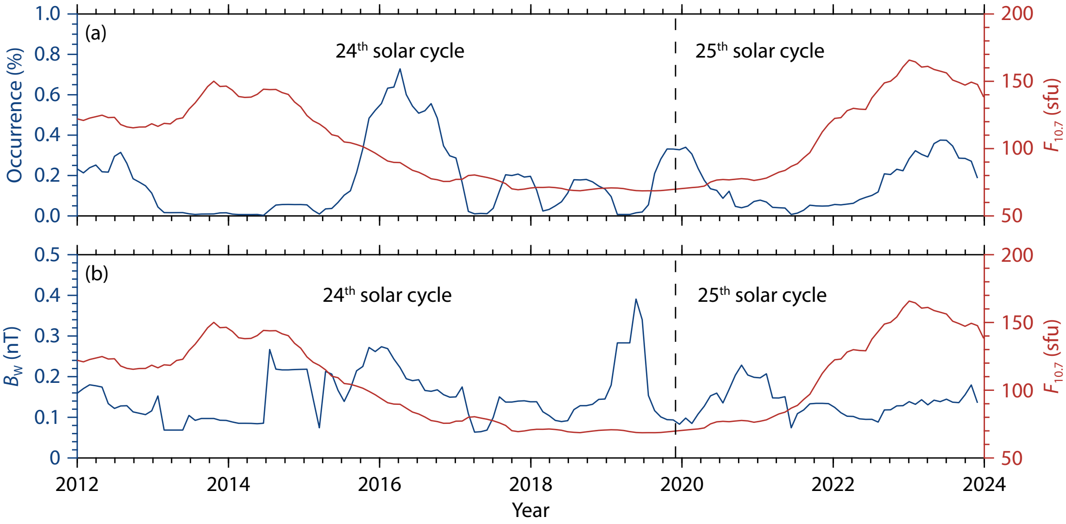

**Figure 9**. Temporal evolution of 1 Hz wave properties and the $F_{10.7}$ index. (a) Occurrence rate (blue curve) and $F_{10.7}$ index (red curve). (b) Wave amplitude (blue curve) and $F_{10.7}$ index (red curve). The vertical dashed black line indicates the boundary between Solar Cycle 24 and Solar Cycle 25.

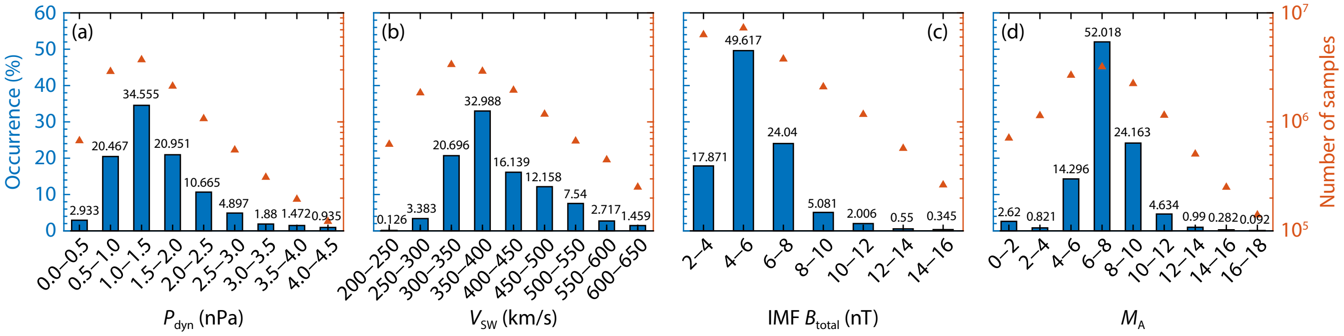

**Figure 10**. Occurrence rates of 1 Hz waves as a function of the (a) solar wind dynamic pressure ($P_{dyn}$); (b) solar wind speed ($V_{SW}$); (c) IMF magnitude ($B_{total}$); and (d) Alfvén Mach number ($M_A$). The orange triangles represent the number of samples in each bin.

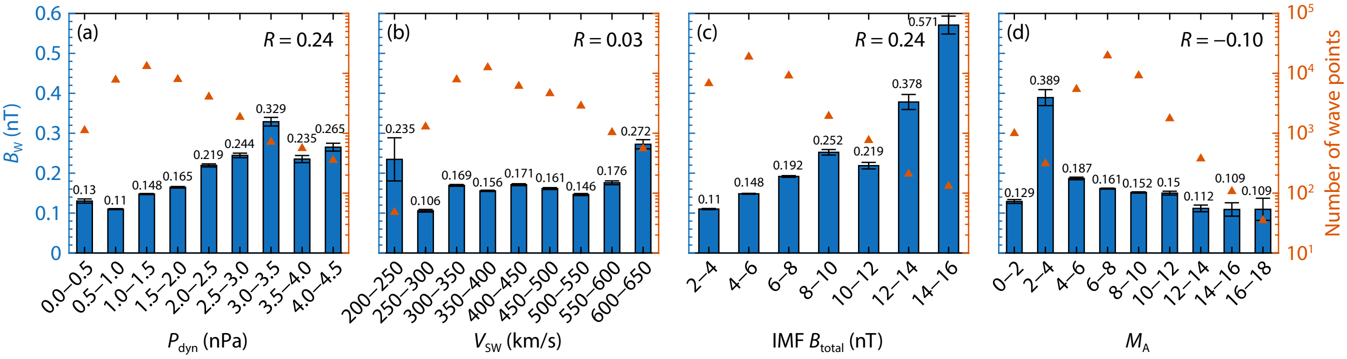

**Figure 11**. Amplitude of 1 Hz waves as a function of the (a) solar wind dynamic pressure ($P_{dyn}$); (b) solar wind speed ($V_{SW}$); (c) IMF magnitude ($B_{total}$); and (d) Alfvén Mach number ($M_A$). The orange triangles represent the number of wave data points in each bin. The error bars represent the standard error of the mean. $R$ represents the correlation coefficient between $B_w$ and each parameter, which is calculated from the full dataset.

$M_A$ = 6–8 (50% of events; Figure 10d).

Wave amplitude dependencies are shown in Figure 11. The blue bars indicate the mean values of $B_W$ in the corresponding solar wind parameter ranges. The correlation coefficient here is calculated from the full dataset. The amplitude increases with $P_{dyn}$ (0.11–0.329 nT), peaking at $P_{dyn}$ = 3–3.5 nPa (Figure 11a). A weak positive correlation with $V_{SW}$ is observed with a correlation coefficient of 0.03 in general. In the range of 500–650 km s$^{-1}$, the amplitude increases from 0.146 nT to 0.272 nT (Figure 11b). The amplitude is positively correlated with $B_{total}$ (Figure 11c) and inversely correlated with $M_A$ for $M_A$ = 4–18 (Figure 11d). Elevated amplitudes at $M_A$ = 2–4 may reflect low event counts (see Figure 10d) with the highest standard error. Caution is warranted in interpreting bins with sparse data (e.g., $V_{SW}$ = 200–250 km s$^{-1}$).

Figure 12 examines the peak frequency ($f_{peak}$) dependence. The blue bars indicate the mean values of peak frequency in the corresponding solar wind parameter ranges. The $f_{peak}$ increases with $P_{dyn}$ (0.991–1.947 Hz; Figure 12a) and $V_{SW}$ (250–650 km s$^{-1}$, peaking at 2.095 Hz; Figure 12b). For $B_{total}$, $f_{peak}$ maximizes at 1.672 Hz within 10–12 nT but lacks a clear trend overall ($\Delta \sim$ 0.5 Hz; Figure 12c). A positive $f_{peak}$–$M_A$ correlation is evident (Figure 12d). These trends collectively indicate that $f_{peak}$ is modulated by upstream solar wind conditions, particularly $P_{dyn}$, $V_{SW}$, and $M_A$.

## 4. Conclusions and Discussion

In this study, we analyze 12 years of ARTEMIS data to investigate the spatial distributions of lunar 1 Hz waves and their dependence on solar wind parameters and the solar cycle. Our findings provide new insights into the generation mechanisms and propagation characteristics of these waves. The key findings are summarized below:

(1) *Spatial distribution and polarization*: 1 Hz waves are primarily observed in the solar wind near the Moon, exhibiting dawn–dusk and north–south asymmetries in both occurrence and amplitude. Amplitudes range from 0.03 to 1 nT, with higher values observed in the terrestrial magnetosheath and in proximity to the lunar dayside. The waves tend to be left-hand polarized with small wave-normal angles. However, near the Moon, particularly on the dayside and around the lunar wake, the waves exhibit a preference for linear polarization, perpendicular propagation, and higher peak frequencies.

(2) *Magnetic connectivity*: The majority (~90%) of observed 1 Hz waves are not magnetically connected to the Moon. The remaining ~10% that are magnetically connected are predominantly located on the dayside and dawn side in SSE coordinates, with a higher occurrence rate than the overall 1 Hz wave population. In selenographic distributions, the footpoints of these magnetically connected waves show a clear positive correlation with the location and strength of lunar magnetic anomalies.

(3) *Solar cycle and solar wind parameter dependence*: The occurrence of 1 Hz waves presents a positive correlation with $F_{10.7}$ during the 2021–2024 period. The amplitude of 1 Hz waves exhibits a positive correlation with $P_{dyn}$ and IMF $B_{total}$, and a negative correlation with $M_A$. The peak frequency shows a positive correlation with $P_{dyn}$, $V_{SW}$, and $M_A$, suggesting a link to upstream solar wind conditions.

The 1 Hz waves are intrinsically right-hand polarized and propagate upstream (Russell, 2007). When they propagate against the solar wind, their polarization is reversed by a sufficient Doppler shift from right-hand polarized to left-hand polarized in the spacecraft frame (Fairfield, 1974). This reversal could explain why the waves near the Moon are more linearly polarized. These Moon-generated waves show original polarization characteristics at first and gradually turn to left-hand polarization during propagation, which fits the ellipticity variation in Figure 4c. Furthermore, we found that many waves in the lunar wake are more linearly polarized, which is due to the absence of solar wind in the lunar wake and less Doppler shift. The wave-normal angle shows a similar distribution as ellipticity, in which the wave with a large wave-normal angle is more linearly polarized (Figures 4c and 5c). Previous studies (Fairfield, 1974; Orlowski and Russell, 1991) have reported that the wave propagating at larger wave-normal angles is less Doppler shifted, which could explain this distribution of ellipticity and wave-normal angle.

As reported in previous studies (e.g., Harada et al., 2015), the non-solar wind ions and some low-frequency waves (including 1 Hz waves) are enhanced on the dawn side. When the Moon is in the solar wind, satellites are more likely connected to the strong magnetic anomalies on the dawn side and reflected ions tend to concentrate on the dawn side. This may explain the dawn–dusk asymmetries found for the occurrence and amplitudes of 1 Hz waves. The north–south asymmetries have also been reported and explained in previous studies (Tsugawa et al., 2011; Lou YQ et al., 2023). These may be caused by the distribution of lunar magnetic anomalies. Those dawn–dusk and north–south asymmetries could be evidence of connection between 1 Hz waves and reflected ions. The amplitudes of 1 Hz waves show similar biased distributions as the magnetic anomalies in the selenographic distributions. Furthermore, Figure 8 directly presents this correlation between the occurrence and amplitude of 1 Hz waves and magnetic anomalies. These asymmetries imply that 1 Hz waves are related to magnetic anomalies and reflected ions.

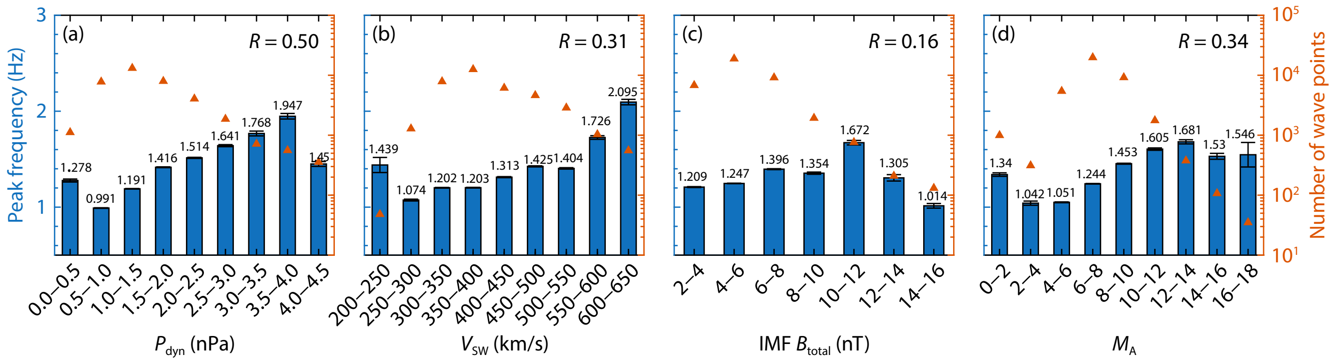

**Figure 12**. Peak frequency of 1 Hz waves as a function of the (a) solar wind dynamic pressure ($P_{dyn}$); (b) solar wind speed ($V_{SW}$); (c) IMF magnitude ($B_{total}$); and (d) Alfvén Mach number ($M_A$). The orange triangles represent the number of wave data points in each bin. The error bars represent the standard error of the mean.

We acknowledge that our connection analysis, which is based on a straight magnetic field line assumption and assesses each data point individually, might underestimate the true number of waves influenced by a connection. The effects of a magnetic connection (e.g., the presence of reflected ions and wave power) can persist even after the spacecraft moves to an unconnected field line. A previous study at Mercury (Le et al., 2013) suggested that wave power on unconnected field lines might persist for ~1 minute after an IMF direction change. This means that waves observed on "unconnected" field lines might still be causally linked to a recent connection. The absence of a direct connection for most waves (90% of unconnected waves) implies a more complex generation and propagation scenario. This could involve (1) waves generated *in situ* in the broader lunar interaction region, (2) waves propagating from connected to unconnected regions, or (3) a potential contribution from remote sources, such as waves generated at Earth's bow shock propagating upstream.

The fact that the dawn–dusk asymmetry persists in the unconnected population suggests a source that is spatially linked to reflected ions but is more diffuse than the narrow flux tubes of connected field lines. This could involve wave generation within a broader region of plasma that has been "conditioned" by reflected ions. The observed wave-normal angles (generally around 30°) allow for propagation across magnetic field lines. Therefore, it is plausible that waves generated on connected field lines could propagate to nearby unconnected regions, where they are subsequently observed. One observational constraint comes from two-probe observations (using both P1 and P2), where a wave event can be seen by both probes. Often, the probe closer to the Moon observes a stronger wave with a clear magnetic connection while the farther probe sees a weaker, unconnected wave. This difference suggests that propagation effects are significant. A detailed analysis comparing the wave vector (***k***) and the magnetic field vector (***B***) would be required for a definitive separation, which is beyond the scope of this statistical study but is an important avenue for future work. We also introduce the possibility of a contribution from waves generated at the terrestrial bow shock, which could act as a diffuse background source and propagate upstream to the Moon's location, although distinguishing them from locally generated lunar waves is challenging. Despite the low percentage of direct connections, we argue that reflected ions are still the most likely primary energy source. The spatial distributions show a clear dawn–dusk asymmetry in wave occurrence and amplitude, which persists even for the unconnected wave population, aligning with previous findings (Halekas et al., 2006; Tsugawa et al., 2011, 2012). This asymmetry strongly mirrors the known distribution of reflected ions, suggesting they are a crucial ingredient for wave generation, even if the waves are generated in a more diffuse region or propagate to unconnected field lines. Other mechanisms, such as electron beams or temperature anisotropies, cannot be ruled out and warrant further investigation. The connected waves may be generated by reflected ions at an altitude of ~30 km within the interaction region (Kurata et al., 2005) and subsequently propagate outward along magnetic field lines (Zhang H et al., 2021).

The weak correlation over the full 12-year interval is indeed affected by sampling or statistical effects. The ARTEMIS probes have eccentric orbits, meaning that the spatial regions sampled near the Moon vary from year to year. In some years (e.g., 2013 and 2014), the orbits spent less time in the regions where 1 Hz waves preferentially occur, leading to very low detected occurrence rates, which can obscure a long-term physical trend. However, the positive correlation observed from 2021 to 2024 may reflect a genuine physical modulation. During this period, the orbital sampling was more consistent, and the wave occurrence did not exhibit the sudden drops to near zero seen in earlier years. Given that upstream solar wind parameters (which our study shows are correlated with wave properties) are known to vary with solar activity, it is physically plausible that the rising phase of Solar Cycle 25 would lead to an increase in wave occurrence.

Previous research on 1 Hz waves at various planets (Russell, 2007; Ruhunusiri et al., 2018) has shown a decrease in wave frequency with increasing heliocentric distance. In this study, we found that some wave properties show a positive dependence on solar wind parameters. For amplitude, the increase in dynamic pressure could block reflected ions propagating upstream concentrating near the Moon, which could lead to the positive correlation between dynamic pressure and wave amplitude. The increasing of IMF $B_{\text{total}}$ leads reflected ions to occupy a smaller region around the Moon and become hard to propagate that far in the upstream and above the flank (Howard et al., 2020). In addition, the increasing of IMF $B_{\text{total}}$ will force ions to gyrate multiple times around the magnetic field with smaller cyclotron radii near the Moon (Howard et al., 2020). This condition could explain that the fewer waves that occur, the higher the amplitude preferred when IMF $B_{\text{total}}$ is strong (6–16 nT). As the results show in Figure 3c, the waves prefer to reach a stronger amplitude around the Moon, where more reflected ions exist and will be concentrated in the near-Moon region with an increase in IMF $B_{\text{total}}$. Furthermore, a previous study on the 1 Hz waves at Mercury and the Earth suggested that low Mach number conditions, compared with high Mach number conditions, will be preferable for the generation of 1 Hz waves (Le et al., 2013). This could explain why the amplitude is weaker with as the Mach number increases. Previous research (Tsugawa et al., 2014) studied the monochromatic characteristics around 1 Hz waves in the spacecraft frame resulting from a Doppler shift. This can be explained by the group-standing condition, according to which the group velocity vector is almost canceled by the solar wind velocity. The wave frequency in the spacecraft frame is Doppler shifted as $\omega' = \omega - kV_{\text{SW}}\cos\theta_{kx}$ (Tsugawa et al., 2014). Here, $k$ and $V_{\text{SW}}$ are the absolute values of $k$ and $V_{\text{SW}}$, and $\theta_{kx}$ is the angle between the wave vector and the sunward direction. We found that the frequency in the spacecraft frame is dependent on the frequency in the plasma frame, the wave vector, and the solar wind velocity vector. Our results show that an obvious positive correlation exists between the peak frequency of the waves and the solar wind velocity. The solar wind velocity will influence the Doppler shift so that it drives the frequency variation of 1 Hz waves. The dispersion relation of the plasma medium influences the intrinsic wave frequency in the plasma frame, which includes the dependence on plasma density and may lead to the dependence on dynamic pressure. For the dependence on the Mach number, this could be due to the relation between the variation in the Mach number and satisfaction of the group-standing condition (Ruhunusiri et al., 2018). These correlations highlight the Moon's unique role as a nonmagnetized body immersed in the solar wind, where crustal fields and surface interactions dominate wave dynamics. Future studies should explore (1) detailed particle observations to identify the sources of waves on both connected and unconnected field lines; (2) numerical simulations to model the interactions among reflected ions, magnetic anomalies, and plasma waves; and (3) comparative studies of 1 Hz waves across planetary environments to elucidate universal mechanisms and unique lunar phenomena. By addressing these open questions, we can advance our understanding of the dynamic plasma environment near the Moon and its implications for space weather and exploration.

## Acknowledgments

This research was supported by the National Natural Science Foundation of China (Grant Nos. 42474217, U2541290, 42174188, 42188101, 42025404, 42330207, and 42578015), the National Key R&D Program of China (Grant Nos. 2022YFF0503700, 2022YFF0503900, and 2025YFF0512500), the Fundamental Research Funds for the Central Universities (Grant No. 242025kf0008), and the Natural Science Foundation of Hubei Province, China (Grant No. 2025AFA030). We acknowledge K. H. Glassmeier, U. Auster, and W. Baumjohann for the use of FGM data and C. W. Carlson and J. P. McFadden for use of ESA data. All ARTEMIS data used are available at http://artemis.ssl.berkeley.edu. We further thank Lianghai Xie for providing the modeled lunar magnetic field results.

## References

Angelopoulos, V. (2011). The ARTEMIS mission. *Space Sci. Rev.*, *165*(1–4), 3–25. https://doi.org/10.1007/s11214-010-9687-2

Angelopoulos, V., Cruce, P., Drozdov, A., Grimes, E. W., Hatzigeorgiu, N., King, D. A., Larson, D., Lewis, J. W., McTiernan, J. M., … Schroeder, P. (2019). The Space Physics Environment Data Analysis System (SPEDAS). *Space Science Reviews 215*(9). https://doi.org/10.1007/s11214-018-0576-4

Auster, H. U., Glassmeier, K. H., Magnes, W., Aydogar, O., Baumjohann, W., Constantinescu, D., Fischer, D., Fornacon, K. H., Georgescu, E., … Wiedemann, M. (2008). The THEMIS fluxgate magnetometer. *Space Sci. Rev.*, *141*(1–4), 235–264. https://doi.org/10.1007/s11214-008-9365-9

Balikhin, M. A., de Wit, T. D., Alleyne, H. S. C. K., Woolliscroft, L. J. C., Walker, S. N., Krasnosel'skikh, V., Mier-Jedrzejeowicz, W. A. C., and Baumjohann, W. (1997). Experimental determination of the dispersion of waves observed upstream of a quasi-perpendicular shock. *Geophys. Res. Lett.*, *24*(7), 787–790. https://doi.org/10.1029/97GL00671

Baumgärtel, K., and Sauer, K. (1995). Support for the shock source hypothesis of upstream whistlers from hall-MHD calculations. *Adv. Space Res.*, *15*(8–9), 93–96. https://doi.org/10.1016/0273-1177(94)00089-J

Fairfield, D. H. (1974). Whistler waves observed upstream from collisionless shocks. *J. Geophys. Res.*, *79*(10), 1368–1378. https://doi.org/10.1029/ja079i010p01368

Farrell, W. M., Fitzenreiter, R. J., Owen, C. J., Byrnes, J. B., Lepping, R. P., Ogilvie, K. W., and Neubauer, F. (1996). Upstream ULF waves and energetic electrons associated with the lunar wake: Detection of precursor activity. *Geophys. Res. Lett.*, *23*(10), 1271–1274. https://doi.org/10.1029/96GL01355

Greenstadt, E. W., Le, G., and Strangeway, R. J. (1995). ULF waves in the foreshock. *Adv. Space Res.*, *15*(8–9), 71–84. https://doi.org/10.1016/0273-1177(94)00087-H

Halekas, J. S., Brain, D. A., Mitchell, D. L., and Lin, R. P. (2006). Whistler waves observed near lunar crustal magnetic sources. *Geophys. Res. Lett.*, *33*(22), L22104. https://doi.org/10.1029/2006GL027684

Harada, Y., Halekas, J. S., Poppe, A. R., Kurita, S., and McFadden, J. P. (2014). Extended lunar precursor regions: Electron-wave interaction. *J. Geophys. Res.: Space Phys.*, *119*(11), 9160–9173. https://doi.org/10.1002/2014JA020618

Harada, Y., Halekas, J. S., Poppe, A. R., Tsugawa, Y., Kurita, S., and McFadden, J. P. (2015). Statistical characterization of the foremoon particle and wave morphology: ARTEMIS observations. *J. Geophys. Res.: Space Phys.*, *120*(6), 4907–4921. https://doi.org/10.1002/2015JA021211

Hoppe, M. M., Russell, C. T., Frank, L. A., Eastman, T. E., and Greenstadt, E. W. (1981). Upstream hydromagnetic waves and their association with backstreaming ion populations: ISEE 1 and 2 observations. *J. Geophys. Res.: Space Phys.*, *86*(A6), 4471–4492. https://doi.org/10.1029/ja086ia06p04471

Hoppe, M. M., Russell, C. T., Eastman, T. E., and Frank, L. A. (1982). Characteristics of the ULF waves associated with upstream ion beams. *J. Geophys. Res.: Space Phys.*, *87*(A2), 643–650. https://doi.org/10.1029/ja087ia02p00643

Howard, S. K., Halekas, J. S., Farrell, W. M., McFadden, J. P., and Glassmeier, K. H. (2017). Identifying ultra low frequency waves in the lunar plasma environment using trajectory analysis and resonance conditions. *J. Geophys. Res.: Space Phys.*, *122*(10), 9983–9993. https://doi.org/10.1002/2017JA024018

Howard, S. K., Halekas, J. S., Farrell, W. M., McFadden, J. P., and Glassmeier, K. -H. (2020). Solar wind and interplanetary magnetic field influence on ultralow frequency waves and reflected ions near the Moon. *J. Geophys. Res.: Space Phys.*, *125*(2), e2019JA027209. https://doi.org/10.1029/2019ja027209

Kurata, M., Tsunakawa, H., Saito, Y., Shibuya, H., Matsushima, M., and Shimizu, H. (2005). Mini-magnetosphere over the Reiner Gamma magnetic anomaly region on the Moon. *Geophys. Res. Lett.*, *32*(24), L24205. https://doi.org/10.1029/2005GL024097

Le, G., Chi, P. J., Blanco-Cano, X., Boardsen, S., Slavin, J. A., Anderson, B. J., and Korth, H. (2013). Upstream ultra-low frequency waves in Mercury's foreshock region: MESSENGER magnetic field observations. *J. Geophys. Res.: Space Phys.*, *118*(6), 2809–2823. https://doi.org/10.1002/jgra.50342

Lin, R. P., Mitchell, D. L., Curtis, D. W., Anderson, K. A., Carlson, C. W., McFadden, J., Acuña, M. H., Hood, L. L., and Binder, A. (1998). Lunar surface magnetic fields and their interaction with the solar wind: Results from lunar prospector. *Science*, *281*(5382), 1480–1484. https://doi.org/10.1126/science.281.5382.1480

Lou, Y. Q., Gu, X. D., Cao, X., Wu, M. Y., Xiao, S. D., Wang, G. Q., Ni, B. B., and Zhang, T. L. (2023). Statistical analysis of lunar 1 Hz waves using ARTEMIS observations. *Astrophys. J.*, *943*(1), 17. https://doi.org/10.3847/1538-4357/aca767

McFadden, J. P., Carlson, C. W., Larson, D., Ludlam, M., Abiad, R., Elliott, B., Turin, P., Marckwordt, M., and Angelopoulos, V. (2008). The THEMIS ESA plasma instrument and in-flight calibration. *Space Sci. Rev.*, *141*(1–4), 277–302. https://doi.org/10.1007/s11214-008-9440-2

Nakagawa, T., Takahashi, Y., and Iizima, M. (2003). GEOTAIL observation of upstream ULF waves associated with lunar wake. *Earth Planets Space*, *55*(9), 569–580. https://doi.org/10.1186/BF03351789

Orlowski, D. S., Crawford, G. K., and Russell, C. R. (1990). Upstream waves at Mercury, Venus and Earth: Comparison of the properties of one hertz waves. *Geophys. Res. Lett.*, *17*(13), 2293–2296. https://doi.org/10.1029/GL017i013p02293

Orlowski, D. S., and Russell, C. T. (1991). Ulf waves upstream of the Venus bow shock: Properties of one-hertz waves. *J. Geophys. Res.: Space Phys.*, *96*(A7), 11271–11282. https://doi.org/10.1029/91ja01103

Orlowski, D. S., Russell, C. T., Krauss-Varban, D., Omidi, N., and Thomsen, M. F. (1995). Damping and spectral formation of upstream whistlers. *J. Geophys. Res.: Space Phys.*, *100*(A9), 17117–17128. https://doi.org/10.1029/95ja00062

Ruhunusiri, S., Halekas, J. S., Espley, J. R., Eparvier, F., Brain, D., Mazelle, C., Harada, Y., Dibraccio, G. A., Thiemann, E. M. B., … Sulaiman, A. H. (2018). One-hertz waves at Mars: MAVEN observations. *J. Geophys. Res.: Space Phys.*, *123*(5), 3460–3476. https://doi.org/10.1029/2017JA024618

Russell, C. T., Childers D. D., and Coleman, P. (1971). Ogo 5 observations of upstream waves in the interplanetary medium: Discrete wave packets. *J*

*Geophys Res*, *76*(4), 845–861. https://doi.org/10.1029/ja076i004p00845

Russell, C. T. (2007). Upstream whistler-mode waves at planetary bow shocks: A brief review. *J. Atmos. Sol. Terr. Phys.*, *69*(14), 1739–1746. https://doi.org/10.1016/j.jastp.2006.11.004

Saito, Y., Yokota, S., Asamura, K., Tanaka, T., Nishino, M. N., Yamamoto, T., Terakawa, Y., Fujimoto, M., Hasegawa, H., … Takahashi, F. (2010). In-flight performance and initial results of plasma energy angle and composition experiment (PACE) on SELENE (Kaguya). *Space Sci. Rev.*, *154*(1–4), 265–303. https://doi.org/10.1007/s11214-010-9647-x

Sawaguchi, W., Harada, Y., Kurita, S., and Nakamura, S. (2022). Spectral properties of whistler-mode waves in the vicinity of the Moon: A statistical study with ARTEMIS. *J. Geophys. Res.: Space Phys.*, *127*(9), e2022JA030582. https://doi.org/10.1029/2022JA030582

Sentman, D. D., Thomsen, M. F., Gary, S. P., Feldman, W. C., and Hoppe, M. M. (1983). The oblique whistler instability in the Earth’s foreshock. *J. Geophys. Res.: Space Phys.*, *88*(A3), 2048–2056. https://doi.org/10.1029/ja088ia03p02048

Shue, J. H., Chao, J. K., Fu, H. C., Russell, C. T., Song, P., Khurana, K. K., and Singer, H. J. (1997). A new functional form to study the solar wind control of the magnetopause size and shape. *J. Geophys. Res.: Space Phys.*, *102*(A5), 9497–9511. https://doi.org/10.1029/97JA00196

Slavin, J. A. and Holzer, R. E. (1981). Solar wind flow about the terrestrial planets 1. Modeling bow shock position and shape. *J. Geophys. Res.: Space Phys.*, *86*(A13), 11401–11418. https://doi.org/10.1029/ja086ia13p11401

Sulaiman, A. H., Gurnett, D. A., Halekas, J. S., Yates, J. N., Kurth, W. S., and Dougherty, M. K. (2017). Whistler mode waves upstream of Saturn. *J. Geophys. Res.: Space Phys.*, *122*(1), 227–234. https://doi.org/10.1002/2016JA023501

Tsugawa, Y., Terada, N., Katoh, Y., Ono, T., Tsunakawa, H., Takahashi, F., Shibuya, H., Shimizu, H., and Matsushima, M. (2011). Statistical analysis of monochromatic whistler waves near the Moon detected by Kaguya. *Ann. Geophys.*, *29*(5), 889–893. https://doi.org/10.5194/angeo-29-889-2011

Tsugawa, Y., Katoh, Y., Terada, N., Ono, T., Tsunakawa, H., Takahashi, F., Shibuya, H., Shimizu, H., Matsushima, M., … Nishino, M. N. (2012). Statistical study of broadband whistler-mode waves detected by Kaguya near the Moon. *Geophys. Res. Lett.*, *39*(16), L16101. https://doi.org/10.1029/2012GL052818

Tsugawa, Y., Katoh, Y., Terada, N., Ono, T., Tsunakawa, H., Takahashi, F., Shibuya, H., Shimizu, H., and Matsushima, M. (2014). Group-standing of whistler mode waves near the Moon. *J. Geophys. Res.: Space Phys.*, *119*(4), 2634–2648. https://doi.org/10.1002/2013JA019585

Tsunakawa, H., Takahashi, F., Shimizu, H., Shibuya, H., and Matsushima, M. (2015). Surface vector mapping of magnetic anomalies over the Moon using Kaguya and Lunar Prospector observations. *J. Geophys. Res.: Planets*, *120*(6), 1160–1185. https://doi.org/10.1002/2014JE004785

Tsurutani, B. T., Southwood, D. J., Smith, E. J., and Balogh, A. (1993). A survey of low frequency waves at Jupiter: The Ulysses encounter. *J. Geophys. Res.: Space Phys.*, *98*(A12), 21203–21216. https://doi.org/10.1029/93ja02586

Tsurutani, B. T., Smith, E. J., Burton, M. E., Arballo, J. K., Galvan, C., Zhou, X. Y., Southwood, D. J., Dougherty, M. K., Glassmeier, K. H., … Chao, J. K. (2001). Oblique “1-Hz” whistler mode waves in an electron foreshock: The Cassini near-Earth encounter. *J. Geophys. Res.: Space Phys.*, *106*(A12), 30223–30238. https://doi.org/10.1029/2001ja900108

Yu, J., Li, L. Y., Cao, J. B., Chen, L., Wang, J., and Yang, J. (2017). Propagation characteristics of plasmaspheric hiss: Van Allen Probe observations and global empirical models. *J. Geophys. Res.: Space Phys.*, *122*(4), 4156–4167. https://doi.org/10.1002/2016JA023372

Zhang, H., Khurana, K. K., Kivelson, M. G., Angelopoulos, V., Wan, W. X., Liu, L. B., Zong, Q. G., Pu, Z. Y., Shi, Q. Q., and Liu, W. L. (2014). Three-dimensional lunar wake reconstructed from ARTEMIS data. *J. Geophys. Res.: Space Phys.*, *119*(7), 5220–5243. https://doi.org/10.1002/2014JA020111

Zhang, H., Fu, S. Y., Pu, Z. Y., Lu, J. Y., Zhong, J., Zhu, C. B., Wan, W. X., and Liu, L. B. (2019). Statistics on the magnetosheath properties related to magnetopause magnetic reconnection. *Astrophys. J.*, *880*(2), 122. https://doi.org/10.3847/1538-4357/ab290e

Zhang, H., Wei, Y., Zhong, J., Zhang, T. X., Liu, L. B., Ni, B. B., Cao, J. B., Fu, S., Chen, Y. D., … Wan, W. X. (2021). Whistler wings and reflected particles during solar wind interaction of lunar magnetic anomalies. *Geophys. Res. Lett.*, *48*(8), e2021GL092425. https://doi.org/10.1029/2021GL092425